Supplement of Atmos. Chem. Phys., 22, 16003–16015, 2022
https://doi.org/10.5194/acp-22-16003-2022-supplement

Atmospheric Chemistry and Physics
Open Access
EGU

Supplement of

Product distribution, kinetics, and aerosol formation from the OH oxidation of dimethyl sulfide under different RO_2 regimes

Qing Ye et al.

Correspondence to: Qing Ye (qingye@ucar.edu) and Jesse H. Kroll (jhkroll@mit.edu)

1. Reaction mechanisms used in the box model

The full DMS + OH reaction scheme used in the box model is presented in Figure 1. Reactions added to the default sulfur chemistry currently in MCMv3.3.1 are given in Table S1.

Table S1: Reactions added to the default sulfur chemistry in MCMv3.3.1. (Jenkin et al., 1997; Saunders et al., 2003) **in the box model**

Gas-phase reactions	k^a	References
$CH_3SCH_2OO \rightarrow OOCH_2SCH_2OOH$ (isomerization)	0.09	Ye *et al.* 2021
$OOCH_2SCH_2OOH \rightarrow HOOCH_2SCHO + OH$	5.8×10^{11} exp(-10155/T + 1080200/T^2)	Wu *et al.* 2015
$OOCH_2SCH_2OOH + NO \rightarrow OCH_2SCH_2OOH + NO_2$	4.9×10^{-12} exp(260/T)	Same as CH_3SCH_2OO in MCMv3.3.1
$OOCH_2SCH_2OOH + HO_2 \rightarrow HOOCH_2SCH_2OOH$	1.13×10^{-12} exp(1300/T)	Same as CH_3SCH_2OO in MCMv3.3.1
$OCH_2SCH_2OOH \rightarrow SCH_2OOH + HCHO$	1×10^6	Same as CH_3SCH_2O in MCMv3.3.1
$HOOCH_2SCHO + OH \rightarrow HOOCH_2SCO$	1.0×10^{-11}	Vermeuel *et al.* 2020
$HOOCH_2SCO \rightarrow CO + HOOCH_2S$	9.2×10^9 exp(−505.4/T)	Wu *et al.* 2015
$HOOCH_2SCO \rightarrow OH + HCHO + OCS$	1.6×10^7 exp(−1468.6/T)	Wu *et al.* 2015
$HOOCH_2S + NO_2 \rightarrow HOOCH_2SO + NO$	6.0×10^{-11} exp(240/T)	Same as CH_3S in MCMv3.3.1
$HOOCH_2S + O_3 \rightarrow HOOCH_2SO + O_2$	1.15×10^{-12} exp(430/T)	Same as CH_3S in MCMv3.3.1
$HOOCH_2SO + O_3 \rightarrow SO_2 + HCHO + OH + O_2$	4.0×10^{-13}	Same as CH_3SO in MCMv3.3.1
$HOOCH_2SO + NO_2 \rightarrow SO_2 + HCHO + OH + NO$	1.2×10^{-11}	Same as CH_3SO in MCMv3.3.1

a: The units of k are s^{-1} for unimolecular reactions and cm^3 $molec^{-1}$ s^{-1} for bimolecular reactions.

2. Instruments

Table S2: S-containing products detected and the corresponding instruments

Formula detected (not including reagent ions)	Assigned species	Vocus PTR-MS	I^--CIMS	NH_4^+- CIMS	AMS	Compact TILDAS
C_2H_6S	Dimethyl sulfide	✓				
C_2H_6SO	Dimethyl sulfoxide	✓		✓		
$C_2H_6SO_2$	Dimethyl sulfone, Methylthiomethyl hydroperoxide	✓		✓		
C_2H_4SO	Methylthioformate	✓		✓		
CH_4SO_2	Methanesulfinic acid	✓	✓	✓		
$C_2H_4SO_3$	Hydroperoxymethyl thioformate		✓	✓		

CH_3SO_6N	Methanesulfonyl peroxynitrate		✓			
CH_2SO_2	Thioacid		✓			
$CH_3SO_2^+$ etc	Methane sulfonic acid				✓	
SO^+, SO_2^+, SO_3^+ etc	Sulfuric acid/Sulfate aerosol				✓	
	Sulfur dioxide					✓

2.1 Vocus PTR-MS measurements

A Vocus Proton-Transfer-Reaction Time-of-Flight Mass Spectrometer (Vocus PTR-MS, Aerodyne Research Inc.) was used to measure the precursor and lightly oxygenated products from the oxidation (see Table S1) with sub-ppt detection limits (Krechmer et al., 2018). The instrument details are documented in Krechmer *et al*. (Krechmer et al., 2018). Reaction mixtures were directly sampled from the chamber at 1 slpm and measured at 1 Hz frequency. The compounds in the mixtures were ionized by proton transfer reactions with the hydronium ion (H_3O^+) and detected as $M{\bullet}H^+$.

The sensitivity of the Vocus PTR-MS to a wide range of compounds was calibrated using two methods. In the first method, the instrument sampled a flow of calibration gas from a cylinder that contained 5 ppb of an array of compounds including acetone, benzene, α-pinene and several other VOCs. This calibration was performed every 4 hours during the experiments. In the second calibration, a liquid calibration system was used to generate known amounts of species that were expected to form in the experiments including DMSO and $DMSO_2$, by quantitatively evaporating the solution containing the compounds of known concentrations into a stream of ultra-zero air that was sampled by the instrument. By varying the concentration of the solution, a four-point calibration was conducted, denoted as the reference sensitivity for DMSO and $DMSO_2$, S_{DMSO_ref} and S_{DMSO2_ref}. The second type of calibration was conducted two times during the middle of the chamber campaign, and the sensitivities to DMSO and $DMSO_2$ were averaged between the two calibrations. The sensitivity uncertainty of DMSO and $DMSO_2$ was determined to be 10% and 3%, respectively, by taking the standard deviation of the sensitivities derived from the two calibrations. Acetone sensitivity using the calibration gas was also calibrated during the second calibration, denoted as $S_{acetone\_ref}$. The instrument sensitivity may vary over time, and therefore, the sensitivity of DMSO (and similarly $DMSO_2$) in every experiment was derived by scaling the acetone reference sensitivity:

$$S_{DMSO\_exp} = S_{DMSO\_ref} \times \frac{S_{acetone\_exp}}{S_{acetone\_ref}}$$

2.2 I^--CIMS measurements

An Iodide Time-of-Flight Chemical Ionization Mass Spectrometer (I^--CIMS) was used to measure more oxidized species in the reaction mixture. A ^{210}Po strip (10 mCi, NRD LLC) was used to ionize methyl iodide vapor from a permeation tube forming I^- as the reagent ions. A 1.8 slpm sample flow taken from the chamber was mixed with a 2 slpm humidified N_2 flow carrying the reagent ions in the ion−molecule reactor.

To calibrate and constrain the sensitivity of the I^--CIMS to a broad range of compounds including products in DMS oxidation, calibrations using authentic standards and the voltage scanning technique (Isaacman-VanWertz et al., 2018; Lopez-Hilfiker et al., 2016) were used. First, the sensitivity of N_2O_5 which represents the maximum sensitivity of the instrument was determined. A known amount of N_2O_5 was formed in the chamber under dry condition by injecting 1-5 ppb of O_3 into the chamber prefilled with 1-2 ppm of NO_2:

$$NO_2 + O_3 \rightarrow NO_2 + O_2$$

$$NO_3 + NO_2 \rightleftarrows N_2O_5$$

Each addition of O_3 was allowed to equilibrate until the $N_2O_5 \bullet I^-$ signal was stable. The total measured signals of N_2O_5 by the I^--CIMS included $N_2O_5I^-$ and NO_3^- ions (Lopez-Hilfiker et al., 2016). Multiple O_3 additions were conducted to derive a multi-point calibration, and the N_2O_5 concentration in the chamber was calculated using the F0AM model. The derived N_2O_5 sensitivity is 12 cps ppt^{-1} (normalized to 10^6 cps reagent ions).

The sensitivities of several organic acids were also calibrated by using the liquid calibration system. Similar to the calibration of Vocus PTR-MS, known concentrations of calibrants were delivered to the I^--CIMS for a multipoint calibration by quickly evaporating the solution containing the calibrants in the liquid calibration system. Voltage scanning was performed during the calibration by changing the voltage between the skimmer and big segment quadrupole to examine the binding energy of the iodide-molecule adduct, denoted as dV50, the voltage at which 50% of the adduct declustered (Isaacman-VanWertz et al., 2018; Lopez-Hilfiker et al., 2016).

Figure S1 shows the relationship between the measured sensitivity and dV50 for compounds calibrated. It is known that succinic acid is measured close to the maximum instrument sensitivity and therefore, it is determined that species with a dV50 ~5V or greater will be detected at the maximum sensitivity. Voltage scanning was also performed every two hours in every experiment for all species measured. Based on the voltage scanning results, the sensitivities of sulfur-containing products were estimated: dV50 for CH_4SO_3 (MSA), CH_2SO_2 (thioacid or sulfene) and CH_3SO_6N (methanesulfonyl peroxynitrate) were 4.7 V, 5.4 V and 9.4 V, respectively; their sensitivities were therefore estimated to be 12 cps ppt^{-1}. The dV50 for $C_2H_4SO_3$ (HPMTF) and CH_4SO_2 (MSIA) were 2.6 V and 2.7 V, respectively, close to the dV50 of HONO, and their sensitivities were estimated to be the same as HONO, 1.0 cps ppt^{-1}.

There are substantial uncertainties for the estimated sensitivities using voltage scanning. Therefore, in Section 3.3 in which the yield of HPMTF was calculated to derive the isomerization rate coefficient (k_{isom}) of the CH_3SCH_2OO radical, a calibration factor was included (Eq. S1 and Eq. S4). However, the fitting in Figure 3(a) is only sensitive to the shape of the curve, and not the absolute value. This helps minimize the effect of uncertainty of the HPMTF calibration on the determination of k_{isom}. Note that in dry experiments, good sulfur closure measurements were obtained from data collected by independently calibrated instruments, and the asymptote value in Figure 3a is close to 1 (1.5), suggesting that our estimated sensitivities were reasonable. To estimate the overall uncertainty in the sulfur closure, a 50% relative standard deviation was applied to individual species measured by the I-CIMS.

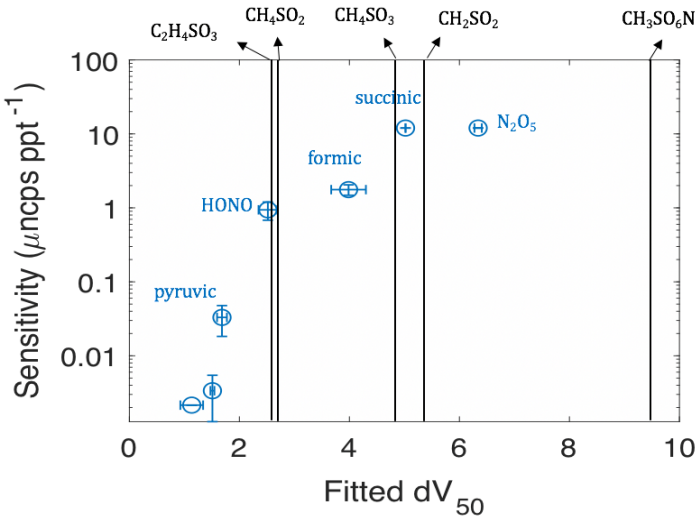

Figure S1: I^--CIMS sensitivity of N_2O_5 and organic acids versus their iodide cluster disassociation voltage derived from voltage scanning. The sensitivities of the sulfur-containing products are determined as the following: $S_{C2H4SO3}$ = 1 cps ppt^{-1}, S_{CH4SO2} = 1 cps ppt^{-1}, S_{CH4SO3} = 12 cps ppt^{-1}, S_{CH2SO2} = 12 cps ppt^{-1}, $S_{CH3SO6N}$ = 12 cps ppt^{-1}, normalized to 10^6 cps reagent ions.

2.3 NH_4^+-CIMS measurements

A time-of-flight chemical ionization mass spectrometer which used ammonium (NH_4^+) as the reagent ion (NH_4^+-CIMS) was also deployed to measured oxygenated products (Zaytsev et al., 2019). Table S2 lists the sulfur-containing species by the NH_4^+-CIMS. The instrument uses a ¼" PFA Teflon sampling line with a flow of 3.5 slpm. The instrument is designed to minimize inlet losses of sampled compounds. The dominant reagent ions are $NH_4^+•(H_2O)n$, (n = 0, 1, 2), and chemical species are detected as ammonium-clusters $NH_4^+•(M)$ through ligand-switching reactions.

Unlike the I^--CIMS, the NH_4^+-CIMS detects HPMTF without the interference from N_2O_5. Figure S2 illustrates that the $C_2H_4SO_3$-$^{12}C_2$ signal measured by both instruments show a consistent time series in Exp. 2a. This confirms that there is negligible N_2O_5 interference in the I^--CIMS measurements of HPMTF used in the total-sulfur analysis.

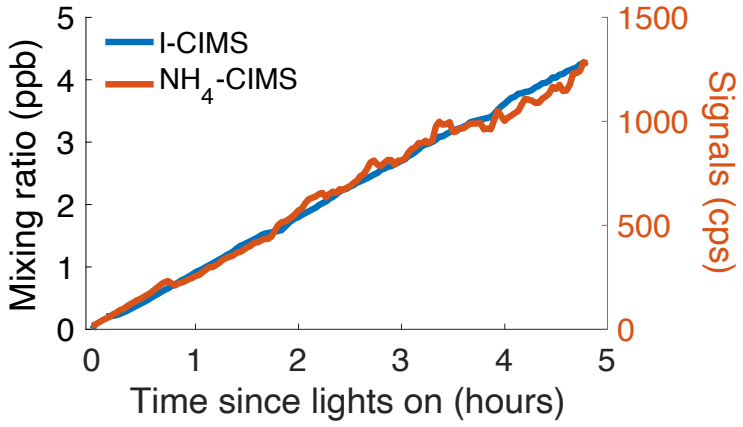

Figure S2: Time series of $C_2H_4SO_3$ (from DMS-$^{12}C_2$) measured by the I^--CIMS and the NH_4^+-CIMS in Exp. 2a.

2.4. Aerodyne Compact Tunable Infrared Laser Direct Absorption Spectrometer (TILDAS)

The SO_2 concentration was measured using an Aerodyne Compact Tunable Infrared Laser Direct Absorption Spectrometer (TILDAS) (McManus et al., 2011; McManus et al., 1995). The single-laser instrument measured SO_2 absorptions near 1352 cm^{-1}, in a 76-m astigmatic multipass absorption cell (AMAC) (McManus et al., 1995). The continuous wave laser was rapidly scanned at kHz rates, and resulting spectra were averaged every second and fit on-the-fly using on board software (TDLWintel). Typical 1-s noise levels were 160 ppt, averaging to < 40 ppt in 100 seconds. The instrument was zeroed every 5 minutes using ultra-zero air, and calibrated using a 5.1 ppm standard diluted into an ultra-zero air overflow from 0-1000 ppb.

2.5 Particle-phase measurements using the aerosol mass spectrometer

Calibration and raw data analysis

The aerosol mass spectrometer (AMS) was calibrated for ionization efficiency using ammonium nitrate. Relative ionization efficiencies (RIE) for NH_4^+ (3.96), SO_4^{2-} (0.92), and MSA (1.20) were calculated using NH_4NO_3, NH_4SO_4, and $NH_4(CH_3SO_3)$ using the ammonium balance method (Hodshire et al., 2019).

Quantification of MSA was performed using SQUIRREL 1.63B and PIKA 1.23B based on the method published by Huang *et al*., 2017 (Huang et al., 2017), where the total mass of MSA is based on a reference spectrum and the distinctive fragment $CH_3SO_2^+$. Since MSA fragmentation has been shown to vary based on instrumental factors (Zorn et al., 2008), a pure MSA spectrum for our instrument was taken from MSA aerosolized into the chamber. The reference spectrum was obtained by summing the high-resolution families that contribute to the MSA spectrum (CHOgt1, CHO1, CH, CS, C_x, SO, HS) and removing others (such as NH) that result from trace ammonia in the chamber/sampling lines. No significant ions except for $CH_3SO_2^+$ were observed at *m/z* 79 in high resolution analysis during the experiments so the entire unit mass was assigned to this ion.

Particles containing $DMSO_2$ were also generated by atomizing a $DMSO_2$ solution and was directly introduced to the AMS. However, no aerosol signals were observed. This is probably because $DMSO_2$ is volatile to semi-volatile (Scholz et al., 2022) and therefore evaporated when entering the chamber. As a result, no aerosol-phase reference spectrum of $DMSO_2$ was obtained. It is expected that at least in the dry experiments, $DMSO_2$ stayed in the gas-phase and did not contribute to the $CH_3SO_2^+$ fragment in the AMS.

For Experiment 4 when the AMS was operated at 800 °C, a reference spectrum for MSA taken at 800 °C was used instead. The fragmentation table in SQUIRREL 1.63B was adjusted according to the reference spectrum.

For experiments in which both ^{12}C- and ^{13}C-DMS were used, this method was modified to account for both isotopes. A reference ^{13}C-MSA spectrum was first derived from the ^{12}C-MSA spectrum by inspection—based on which ions contain carbon—since no pure sample is easily available. Next, the ^{12}C / ^{13}C isotope ratio, which remained constant throughout each experiment, was derived based on high resolution fitting at m/z 96 and m/z 97 where few ions interfered with the $^{12}CH_4SO_3^+$

and $^{13}CH_4SO_3^+$ signals. The key peak for ^{13}C-MSA ($^{13}CH_3SO_2^+$) was easily distinguished from SO_3^+ in high resolution and the ratio of these ions was used to calculate the total ^{13}C-MSA mass using the reference spectrum and the unit mass resolution frag table. The signal from the key peak for ^{12}C-MSA ($^{12}CH_3SO_2^+$) is estimated based on the ^{12}C / ^{13}C isotope ratio and the $^{13}CH_3SO_2^+$ signal; total ^{12}C-MSA mass is then calculated as above based on the derived $^{12}CH_3SO_2^+$ signal.

Corrections

Particle wall loss was accounted for when estimating the concentration of aerosol-phase products. Particle wall loss rate was expected to be faster during the beginning of the experiment and gradually decreased as the experiment proceeds due to the growth of the particles. The estimate of particle wall loss rate was performed by measuring the loss rate of particle containing 2:1 mix of H_2SO_4 and MSA by aerosolizing the solution containing the mixture into the chamber. This particle composition roughly matched that of the observed products. AMS results corrected by this single mass-based wall loss rate coefficient were taken as the "best estimate", which was 5.74×10^{-5} s^{-1}, and was applied for wall loss correction for entire experiments based on Wang *et al*. (Wang et al., 2018). Upper (1.59×10^{-4} s^{-1}) and lower (4.58×10^{-5} s^{-1}) bounds for this wall loss correction were additionally calculated based on the faster average loss rate of the $NaNO_3$ seed particles and the slower average rate at the end of experimental particle losses, respectively. Particle mass concentrations calculated using the upper and lower bounds of wall loss correction were included in the overall uncertainty of the sulfur closure.

Additionally, due to the presence of some particles below the optimal AMS transmission size range, a small correction to the total AMS mass was applied based on the SMPS size distribution and the AMS transmission efficiency curve (Guo et al., 2021), under the assumption that these particles had the same chemical composition. This was done by calculating and correcting for the fraction of the SMPS signal that would not be detected by the AMS. This correction increased calculated mass by an average of 2%. During high-RH experiments, a diffusion dryer was placed upstream of aerosol measurements to remove effects of RH in particle quantifications. By combining the AMS and SMPS data from experiments with a high aerosol yield, the AMS collection efficiency (CE) was estimated assuming spherical particles without voids. The CE for Exp. 1 was estimated to be ~ 0.5, consistent with the previous DMS study published from our group (Ye et al., 2021). The CE for Exp. 4 was ~ 0.3. The lower CE was probably due to the increased particle bounce caused by the sodium chloride seed particles. For the low-aerosol-yield experiments which used the same seed particles as in Exp. 1, a collection efficiency of 0.5 was applied.

3. Estimation of HPTMF vapor pressure and chamber wall loss

Currently there is no reported experimentally measured saturation vapor pressure of HPMTF, C_{HPMTF}, under room temperature. Here, C_{HPMTF} is estimated using two methods. In the first method, the pure component vapor pressure of HPMTF is estimated by based on Compernolle *et al*. (Compernolle et al., 2011) calculated by UManSysProp (http://umansysprop.seaes.manchester.ac.uk/). The estimated C_{HPMTF} is ~ 1×10^8 μg m^{-3}. In the second method, C_{HPMTF} is estimated based on the vapor pressure of DMS which is ~500 mmHg at room temperature (NIST webBook). The addition of the aldehyde group and the hydroperoxide group are expected to lower the vapor pressure by ~1 and ~2.2 decades, respectively (Capouet and Muller, 2006; Pankow and Asher, 2008). Thus, C_{HPMTF} is estimated to be on the order of 1×10^6 μg m^{-3}. Both methods suggest that

C_{HPMTF} is at least two orders of magnitudes greater than the equivalent organic mass of the chamber wall, C_w, which is on the order of 1×10^4 μg m^{-3} (Krechmer et al., 2016). Therefore, only a very small amount (~1% or less) of HPTMF is expected to be deposited onto the chamber wall under dry condition.

4. Determination of k_{isom} of CH_3SCH_2OO

In Exp.3, the oxidation was initiated by H_2O_2 photolysis with 3 ppb of NO in the chamber. Later, different amounts of HONO or NO was injected into the chamber several times to perturb the chemistry of the RO_2 radicals, and in particular decreasing its τ_{bi}. Each perturbation lasted for ~10 minutes, and the branching fraction of the CH_3SCH_2OO radicals that undergo isomerization, f_{isom}, was determined by using the yield of HPMTF in the abstraction channel from the measurements:

$$Y_{HPMTF} = f_{isom} = \frac{a_{Cal} \times \Delta HPMTF}{\Delta DMS \times f_{abs}}. \qquad \text{Eq. S1}$$

In Figure S7 in which the loss of HPMTF via OH oxidation is not considered, ΔHPMTF is simply the change in the measured HPMTF concentration, $\Delta HPMTF_{meas}$. When taking loss by OH oxidation into account, $\Delta HPMTF = \Delta HPMTF_{meas} + \int k_{HPMTF+OH} \times \Delta[HPMTF][OH]\, dt$. Here, 2.1×10^{-11} cm^3 molec^{-1} s^{-1} is used as $k_{HPMTF+OH}$ derived from our measurements.

f_{isom} is also determined by the rate coefficient of the isomerization channel and the bimolecular channels of the CH_3SCH_2OO radical:

$$f_{isom} = \frac{k_{isom}}{k_{isom} + k_{bi}} \qquad \text{Eq. S2}$$

Here, k_{bi} is the bimolecular rate of CH_3SCH_2OO with HO_2 and NO, derived from

$$k_{bi} = \frac{1}{\tau_{bi}} = k_{HO_2}[HO_2] + k_{NO}[NO] \qquad \text{Eq. S3}$$

Taken together, k_{isom} can be estimated by fitting the following equation from the perturbations:

$$Y_{HPMTF} = \frac{1}{a_{Cal}} \times \frac{k_{isom}}{k_{isom} + \frac{1}{\tau_{bi}}} \qquad \text{Eq. S4}$$

Here, f_{abs} = 0.65, which is based on the branching fraction of the abstraction channel under the temperature in this work (Barnes et al., 2006). A calibration factor, a_{cal}, was included as a parameter to account for the calibration uncertainty of HPMTF in the measurements; however its value has no impact on the inflection point of the fitted curve in Figure 3a. The initial concentration of NO in each perturbation was constrained by the measurements, and the subsequent change of NO was derived from F0AM simulations. [HO_2] was also derived from F0AM simulations, and k_{HO_2} and k_{NO} were taken from MCM_V3.3.1 (Jenkin et al., 1997; Saunders et al., 2003). [NO] and [HO_2] were averaged for each of the 10-minute period.

5. Other supporting figures

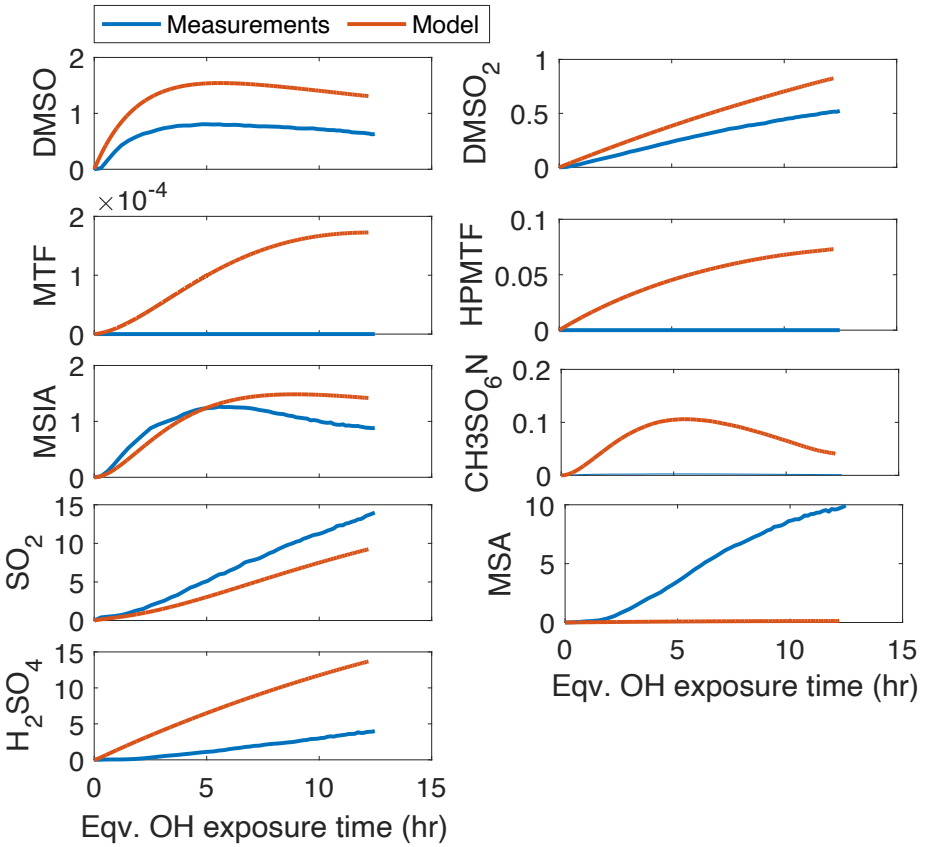

Figure S3: Measurement-model comparison of individual sulfur-containing products under the high-NO condition (Exp. 1). Concentrations (y axis) are in ppb S.

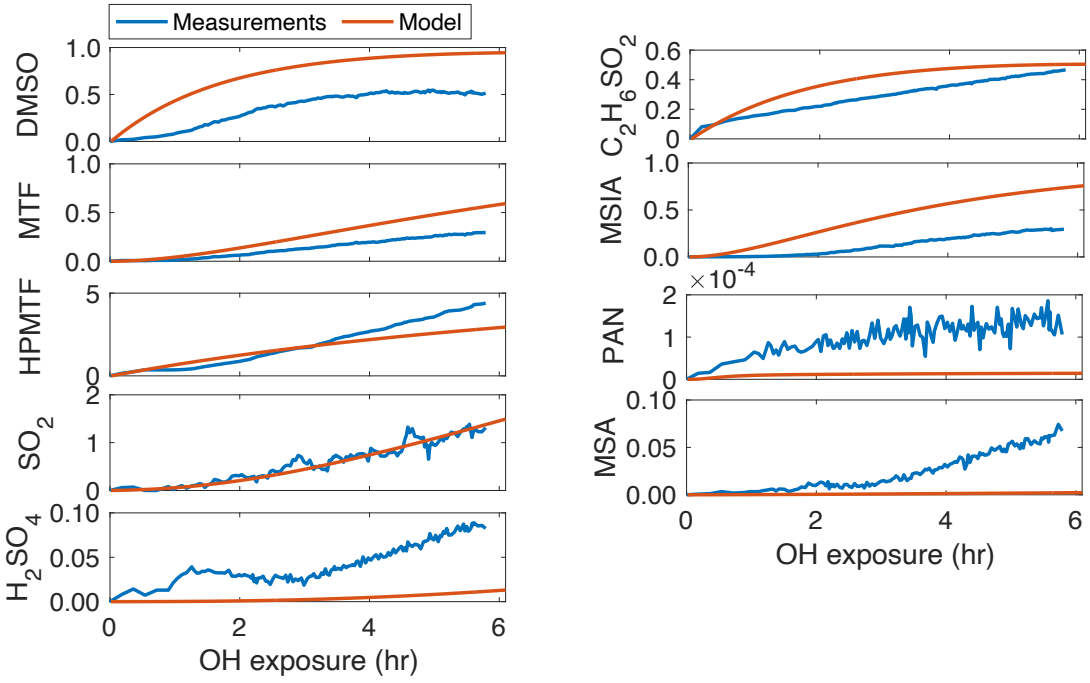

Figure S4: Measurement-model comparison of individual sulfur products from DMS-^{12}C oxidation under the low-NO condition (Exp. 2a). Concentrations (y axis) are in ppb S.

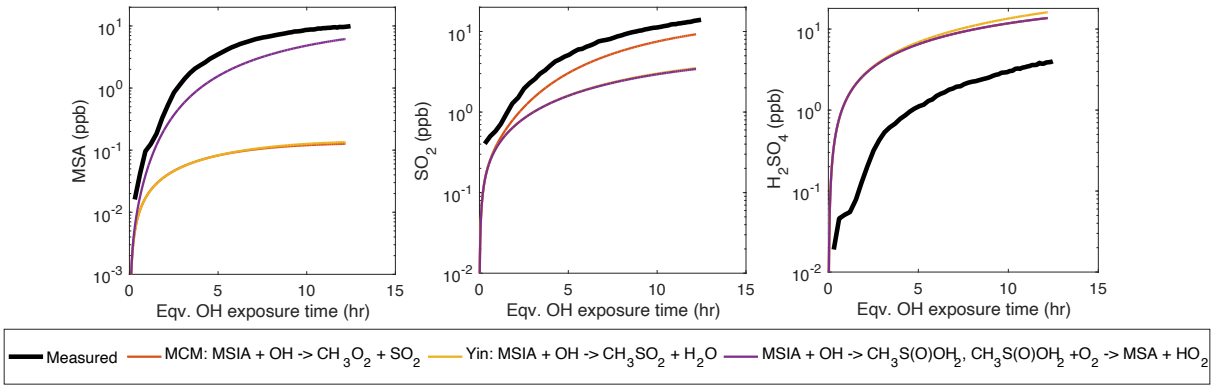

Figure S5: Measured and modeled MSA, SO_2 and sulfuric acid concentrations in different scenarios of MSIA reaction rate constants for Exp. 1 (high-NO). Black: measured concentrations in Exp. 1. Red: modeled concentrations using default MCM mechanism of MSIA + OH → CH_3O_2 + SO_2 with $k_{MSIA+OH}$ = 9×10^{-11} cm^3 molec^{-1} s^{-1}. Yellow: modeled concentrations using MSIA + OH abstraction reaction forming CH_3SO_2 + H_2O with $k_{MSIA+OH}$ = 1.6×10^{-11} cm^3 molec^{-1} s^{-1} used in Yin et al. (1990). Purple: modeled concentrations using MSIA + OH → $CH_3S(O)(OH)_2$ with $k = 9 \times 10^{-11}$ cm^3 molec^{-1} s^{-1} and $CH_3S(O)(OH)_2$ + O_2 → MSA + HO_2 with $k = 1.3 \times 10^{-12} \times \exp(-330/T) \times 0.21 \times M$ (taken from MCM from HSO_3 + O_2 → SO_3 + HO_2).

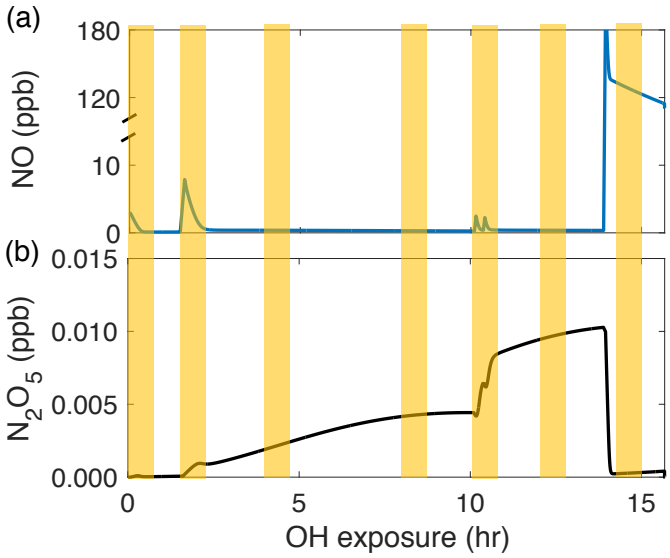

Figure S6: Time series of (a) NO and (b) N_2O_5 in Experiment 3. The initial concentration of NO of every injection was constrained by the measurements and the remaining decay was predicted by the model (there were large measurement uncertainties in the sub-ppb range in the NO-NO_2-NO_x analyzer). Concentration of N_2O_5 is from the model. Yellow stripes indicate the 10-minute periods used in k_{isom} estimation (Figure 3a). Increases in N_2O_5 can lead to interferences in the HPMTF-$^{12}C_2$ signal in the I^--CIMS spectra.

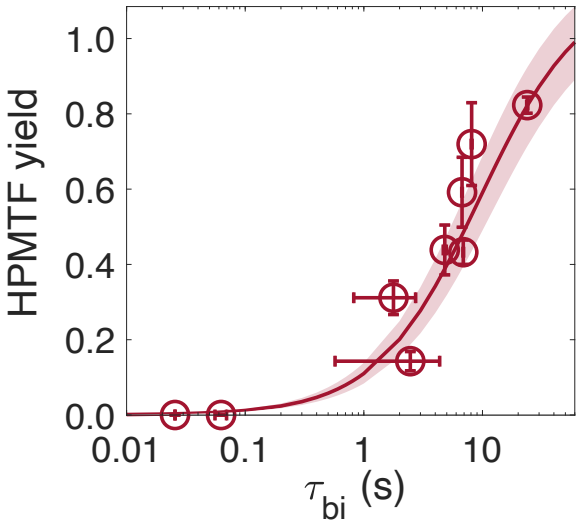

Figure S7: Yields of HPMTF-$^{13}C_2$ as a function of RO_2 bimolecular lifetime without considering HPMTF + OH. The derived fitted k_{isom} = 0.11 ± 0.02 s^{-1}.

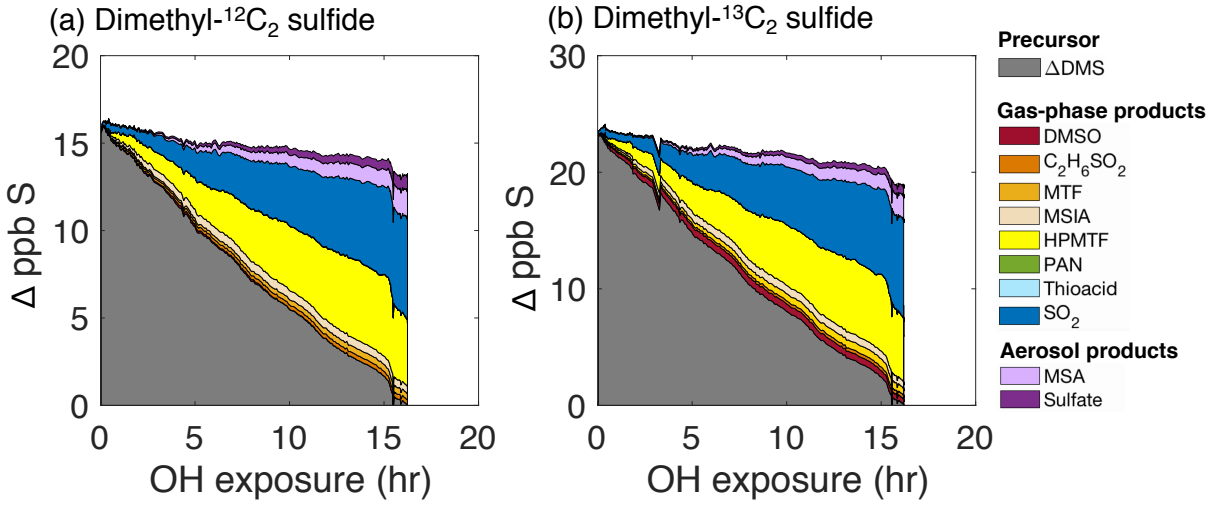

Figure S8: Measurements of total sulfur distribution of (a) DMS-$^{12}C_2$ and (b) DMS-$^{13}C_2$ in Exp. 3.

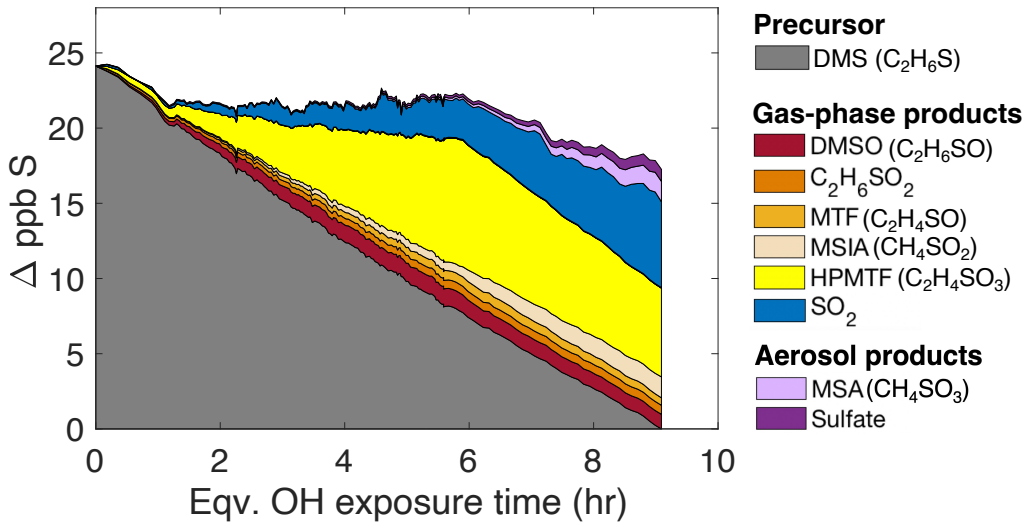

Figure S9: Measured total sulfur distribution for the entire Exp. 2 (DMS-$^{12}C_2$ + DMS-$^{13}C_2$).

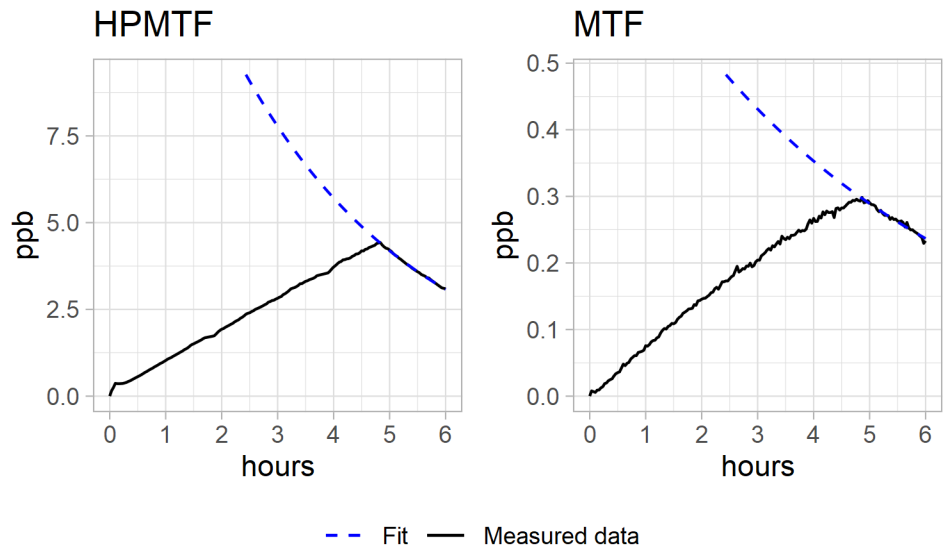

Figure S10: Fittings of HPMTF and MTF decays in Exp. 2b to derive $k_{OH+HPMTF}$ and k_{OH+MTF}.

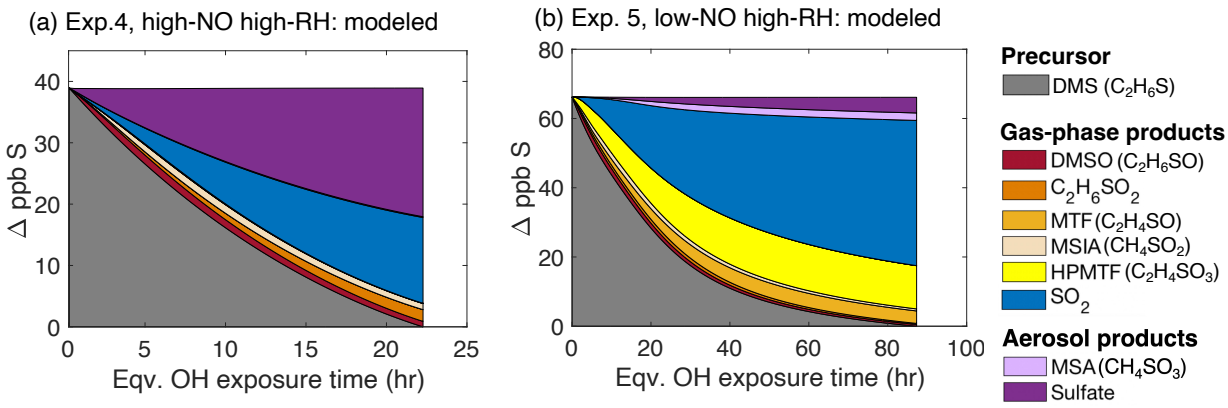

Figure S11: (a) Modeled product distribution of Exp. 4. (b) Modeled product distribution of Exp. 5.

References:

Barnes, I., Hjorth, J. and Mihalapoulos, N.: Dimethyl sulfide and dimethyl sulfoxide and their oxidation in the atmosphere, Chem. Rev., 106, 940–975, https://doi.org/10.1021/cr020529+, 2006.

Capouet, M., and J-F. Müller.: A group contribution method for estimating the vapour pressures of α-pinene oxidation products, Atmos. Chem. Phys., 6, 1455–1467, https://doi.org/10.5194/acp-6-1455-2006, 2006.

Compernolle S., Ceulemans, K., Müller, J.F.: EVAPORATION: a new vapor pressure estimation method for organic molecules including non-additivity and intramolecular interactions, Atmos. Chem. Phys., 11, 9431-9450, https://doi.org/10.5194/acp-11-9431-2011, 2011.

Guo, H., Campuzano-Jost, P., Nault, B. A., Day, D. A., Schroder, J. C., Kim, D., Dibb, J. E., Dollner, M., Weinzierl, B., and Jimenez, J. L.: The importance of size ranges in aerosol instrument intercomparisons: a case study for the Atmospheric Tomography Mission, Atmos. Meas. Tech., 14, 3631–3655, https://doi.org/10.5194/amt-14-3631-2021, 2021.

Hodshire, A. L., Campuzano-Jost, P., Kodros, J. K., Croft, B., Nault, B. A., Schroder, J. C., Jimenez, J. L. and Pierce, J. R.: The potential role of methanesulfonic acid (MSA) in aerosol formation and growth and the associated radiative forcings, Atmos. Chem. Phys., 19, 3137–3160, https://doi.org/10.5194/acp-19-3137-2019, 2019.

Huang, S., Poulain, L., Pinxteren, D. Van, Pinxteren, M. Van, Wu, Z., Herrmann, H. and Wiedensohler, A.: Latitudinal and Seasonal Distribution of Particulate MSA over the Atlantic using a Validated Quantification Method with HR-ToF-AMS, Environm. Sci. & Technol., 51, 418–426, https://doi.org/10.1021/acs.est.6b03186, 2017.

Isaacman-Vanwertz, G., Massoli, P., O'Brien, R., Lim, C., Franklin, J. P., Moss, J. A., Hunter, J. F., Nowak, J. B., Canagaratna, M. R., Misztal, P. K., Arata, C., Roscioli, J. R., Herndon, S. T., Onasch, T. B., Lambe, A. T., Jayne, J. T., Su, L., Knopf, D. A., Goldstein, A. H., Worsnop, D. R. and Kroll, J. H.: Chemical evolution of atmospheric organic carbon over multiple generations of oxidation, Nat. Chem., 10, 462–468, https://doi.org/10.1038/s41557-018-0002-2, 2018.

Jenkin, M. E., Saunders, S. M. and Pilling, M. J.: The tropospheric degradation of volatile organic compounds: a protocol for mechanism development, Atmos. Environ., 31, 81–104, 1997.

Krechmer, E. J., Lopez-Hilfiker, F., Koss, A., Hutterli, M., Stoermer, C., Deming, B., Kimmel, J., Warneke, C., Holzinger, R., Jayne, J., Worsnop, D., Fuhrer, K., Gonin, M. and Gouw, J. De: Evaluation of a new reagent-ion source and focusing ion-molecule reactor for use in proton-transfer-reaction mass spectrometry, Anal. Chem., 90, 12011–12018, https://doi.org/10.1021/acs.analchem.8b02641, 2018.

Krechmer, E. J., Pagonis, D., Ziemann, P. J., Jimenez, J. L.: Quantification of gas-wall partitioning in Teflon environmental chambers using rapid bursts of low-volatility oxidied species generated in situ, Environ. Sci. Technol, 50, 5757-5765, https://doi.org/10.1021/acs.est/6b00606, 2016.

Lopez-Hilfiker, F. D., Iyer, S., Mohr, C., Lee, B. H., D'ambro, E. L., Kurtén, T. and Thornton, J. A.: Constraining the sensitivity of iodide adduct chemical ionization mass spectrometry to multifunctional organic molecules using the collision limit and thermodynamic stability of iodide ion adducts, Atmos. Meas. Tech., 9, 1505–1512, https://doi.org/10.5194/amt-9-1505-2016, 2016.

McManus, J.B., Zahniser, M.S., Nelson, D.D., McGovern, R.M., Agnese, M. and Brown, W.F.: Compact Quantum Cascade Laser Instrument for High Precision Trace Gas Measurements. In Optical Instrumentation for Energy and Environmental Applications (p. EThC2). Optica Publishing Group, https://doi.org/10.1364/E2.2011.EThC2, 2011, November.

McManus, J.B., Kebabian, P.L. and Zahniser, M.S.: Astigmatic mirror multipass absorption cells for long-path-length spectroscopy. Applied Optics, 34, 3336-3348, 1995.

Novak, G. A., Fite, C. H., Holmes, C. D., Veres, P. R., Neuman, J. A., Faloona, I., Thornton, J. A., Wolfe, G. M., Vermeuel, M. P., Jernigan, C. M., Peischl, J., Ryerson, T. B., Thompson, C. R., Bourgeois, I., Warneke, C., Gkatzelis, G. I., Coggon, M. M., Sekimoto, K., Bui, T. P., Dean-Day, J., Diskin, G. S., DiGangi, J. P., Nowak, J. B., Moore, R. H., Wiggins, E. B., Winstead, E. L., Robinson, C., Thornhill, K. L., Sanchez, K. J., Hall, S. R., Ullmann, K., Dollner, M., Weinzierl, B., Blake, D. R. and Bertram, T. H.: Rapid cloud removal of dimethyl sulfide oxidation products limits SO_2 and cloud condensation nuclei production in the marine atmosphere, Proc. Natl. Acad. Sci., 118, https://doi.org/10.1073/PNAS.2110472118, 2021.

Pankow, J. F. and Asher, W. E.: SIMPOL.1: a simple group contribution method for predicting vapor pressures and enthalpies of vaporization of multifunctional organic compounds, Atmos. Chem. Phys., 8, 2773–2796, https://doi.org/10.5194/acp-8-2773-2008, 2008.

Saunders, S. M., Jenkin, M. E., Derwent, R. G. and Pilling, M. J.: Protocol for the development of the Master Chemical Mechanism, MCM v3 (Part A): Tropospheric degradation of non-aromatic volatile organic compounds, Atmos. Chem. Phys., 3, 161–180, https://doi.org/10.5194/acp-3-161-2003, 2003.

Scholz, W., Shen, J., Aliaga, D., Wu, C., Carbone, S., Moreno, I., Zha, Q., Huang, W., Heikkinen, L., Jaffrezo, J.L. and Uzu, G., Measurement Report: Long-range transport and fate of DMS-oxidation products in the free troposphere derived from observations at the high-altitude research station Chacaltaya (5240 m asl) in the Bolivian Andes. EGUsphere [preprint], https://doi.org/10.5194/egusphere-2022-887, 2022.

Vermeuel, M. P., Novak, G. A., Jernigan, C. M. and Bertram, T. H.: Diel Profile of Hydroperoxymethyl Thioformate: Evidence for Surface Deposition and Multiphase Chemistry, Environ. Sci. Technol., 54, 12521–12529, https://doi.org/10.1021/acs.est.0c04323, 2020.

Wang, N., Jorga, S. D., Pierce, J. R., Donahue, N. M. and Pandis, S. N.: Particle wall-loss

correction methods in smog chamber experiments, Atmos. Meas. Tech., 11, 6577–6588, https://doi.org/10.5194/amt-11-6577-2018, 2018.

Wu, R., Wang, S. and Wang, L.: New mechanism for the atmospheric oxidation of dimethyl sulfide. The importance of intramolecular hydrogen shift in a CH_3SCH_2OO radical, J. Phys. Chem. A, 119, 112–117, https://doi.org/10.1021/jp511616j, 2015.

Ye, Q., Goss, M. B., Isaacman-Vanwertz, G., Zaytsev, A., Massoli, P., Lim, C., Croteau, P., Canagaratna, M., Knopf, D. A., Keutsch, F. N., Heald, C. L. and Kroll, J. H.: Organic Sulfur Products and Peroxy Radical Isomerization in the OH Oxidation of Dimethyl Sulfide, ACS Earth Sp. Chem., 5, 2013–2020, https://doi.org/10.1021/acsearthspacechem.1c00108, 2021.

Yin, F., Grosjean, D. and Seinfeld, J. H.: Photooxidation of Dimethyl Sulfide and Dimethyl Disulfide. I: Mechanism Development, J. Atmos. Chem., 11, 309–365, 1990.

Zaytsev, A., Breitenlechner, M., Koss, A. R., Lim, C. Y., Rowe, J. C., Kroll, J. H. and Keutsch, F. N.: Using collision-induced dissociation to constrain sensitivity of ammonia chemical ionization mass spectrometry (NH_4^+ CIMS) to oxygenated volatile organic compounds, Atmos. Meas. Tech., 12, 1861–1870, https://doi.org/10.5194/amt-12-1861-2019, 2019.

Zorn, S. R., Drewnick, F., Schott, M., Hoffmann, T. and Borrmann, S.: Characterization of the South Atlantic marine boundary layer aerosol using an aerodyne aerosol mass spectrometer, Atmos. Chem. Phys., 8, 4711–4728, https://doi.org/10.5194/acp-8-4711-2008, 2008.